Searching for sub-kilometer TNOs using Pan-STARRS video mode lightcurves: Preliminary study and evaluation using engineering data

J.-H. Wang[1,2], P. Protopapas[3,4], W.-P. Chen[2], C. R. Alcock[3], W. S. Burgett[6], T. Dombeck[5]
J. S. Morgan[6], P. A. Price[6], and J. L. Tonry[6]

ABSTRACT

We present a pre-survey study of using Pan-STARRS high sampling rate video mode guide star images to search for TNOs. Guide stars are primarily used by Pan-STARRS to compensate for image motion and hence improve the point spread function. With suitable selection of the guide stars within the Pan-STARRS 7 deg^2 field of view, the lightcurves of these guide stars can also be used to search for occultations by TNOs. The best target stars for this purpose are stars with high signal-to-noise ratio (SNR) and small angular size. In order to do this, we compiled a catalog using the SNR calculated from stars with $m_{\rm V} < 13$ mag in the Tycho2 catalog then cross matched these stars with the 2MASS catalog and estimated their angular sizes from $(V-K)$ color. We also outlined a new detection method based on matched filter that is optimized to search for diffraction patterns in the lightcurves due to occultation by sub-kilometer TNOs. A detection threshold is set to compromise between real detections and false positives. Depending on the theoretical size distribution model used, we expect to find up to *a hundred events* during the three-year life time of the Pan-STARRS-1 project. The high sampling (30 Hz) of the project facilitates detections of small objects (as small as 400 m), which are numerous according to power law size distribution, and thus allows us to verify various models and further constrain our understanding of the structure in the outer reach of the Solar System. We have tested the detection algorithm and the pipeline on a set of *engineering* data (taken at 10 Hz in stead of 30 Hz). No events were found within the engineering data, which is consistent with the small size of the data set and the theoretical models. Meanwhile, with a total of ~ 22 star-hours video mode

email: jhwang@asiaa.sinica.edu.tw, pprotopapas@cfa.harvard.edu

[1]Institute of Astronomy and Astrophysics, Academia Sinica. P.O. Box 23-141, Taipei 106, Taiwan

[2]Institute of Astronomy, National Central University, No. 300, Jhongda Rd, Jhongli City, Taoyuan County 320, Taiwan

[3]Harvard-Smithsonian Center for Astrophysics, 60 Garden Street, Cambridge, MA 02138

[4]Initiative in Innovative Computing, School of Engineering and Applied Sciences, 29 Oxford Street, Cambridge, MA 02138

[5]Physics Department, University of Hawaii, 2680 Woodlawn Drive, Honolulu, HI, 96822

[6]Institute for Astronomy, University of Hawaii, 2680 Woodlawn Drive, Honolulu, HI, 96822

data ($|\beta| < 10°$), we are able to set an upper limit of $N(> 0.5 \text{ km}) \sim 2.47 \times 10^{10}$ deg^{-2} at 95% confidence limit.

1. Introduction

Since the first Kuiper Belt object (not including Pluto) was discovered in 1992 (Jewitt & Luu 1993), more than 1000 trans-Neptunian objects (TNOs) have been found[1]. A picture is emerging of the principal characteristics of the TNOs that is rich in information but leaves many unanswered questions. For example, a number of dynamical groups have been identified: classical, resonant, scattered disk (Luu et al. 1997), and more recently the extended scattered disk (Gladman et al. 2002). What is the number and size distribution of the smaller objects of these dynamical groups? Is there an extension of the Kuiper Belt beyond 50 AU comprising bodies too small to have been detected in direct surveys? Meanwhile, could a possible close stellar encounter in the early history of the Solar System (Allen et al. 2001; Trujillo et al. 2001; Bernstein et al. 2004; Fuentes & Holman 2008) be responsible for the mass deficit and the depletion of larger objects (D > 150 km) beyond 50 AU?

The size distribution of these small TNOs provides important clues to the dynamical evolution of the early Solar System. Kilometer-size TNOs with 4% albedo are expected to have $M_{\rm R} \gtrsim 30$, which is still way below the detection limit of the largest ground-based telescopes. Yet the vast majority of the TNO population is beyond the limit of direct observation –for example, the Keck pencil beam survey (Chiang & Brown 1999) has a detection limit of $M_{\rm R} \approx 27.5$.

A number of authors (Bailey 1976; Roques & Moncuquet 2000) have suggested the possibility of detecting TNOs by stellar occultation. An occultation manifests itself as the shadow created by a TNO occulting a background star sweeping across the Earth, causing flux reduction in the lightcurve. Hence, as opposed to direct observation, stellar occultation by TNOs provides a unique way of detecting kilometer to sub-kilometer size objects in the foreseeable future. Recently a few groups have attempted to search for occultations by TNOs (Roques et al. 2006; Bickerton et al. 2008; Lehner et al. 2009; Zhang et al. 2008; Bianco et al. 2009; Bickerton et al. 2009), but no real detection has been confirmed yet.

Projects committed to search for TNOs by occultation either do not have adequate time resolution, observe too few stars with good SNR or do not have enough observing time. These projects do a blind search for occultations, and these events are rare due to the reasons mentioned above. Therefore, the key to a successful detection is to have high sampling ($\geq$ 20 Hz), high signal to noise ratio of background stars (SNR $\geq$ 80), small stellar angular sizes ($\leq$ 0.1 mas) and, most importantly, many star-hours of observations (> a few hundred thousands).

[1]See http://www.cfa.harvard.edu/iau/lists/TNOs.html for a list of these objects.

The Panoramic Survey Telescope and Rapid Response System (Pan-STARRS) is a project consisting of 4 telescopes that can cover over 6000 deg^2 per night or scan the whole visible sky from Hawaii (3π) in a week to a detecting limit $\sim 24^{\rm th}$ magnitude. Pan-STARRS prototype telescope (PS1) will monitor up to 60 guide stars in a very high sampling rate video mode. We have compiled a list which allows us to select guide stars from anywhere in the field; guide stars could be in any of the 64×64 OTCCDs (see §2) and read at $\sim$ 30 Hz. Each field will have multiple choices of guide stars that were ranked based on the predicted event rates, which depend on their SNRs and angular sizes. By properly selecting guide stars, the Pan-STARRS video mode images would be ideal for searching TNOs.

In the next section, we briefly describe the Pan-STARRS system. In §3 and §4 we discuss the diffraction profiles and present our detection algorithm. In § 5 we describe the prediction of stellar angular size using $(V-K)$ color. In §6 we estimate the number of expected events based on different number density estimations, sampling rates and stellar angular sizes. The methodology and compilation of the guide star list is in §7. In §8, we show and describe the quality of the engineering data obtained in fall 2008. Conclusions are in the final section.

2. Pan-STARRS-1 system

The full version of Pan-STARRS will contain four identical telescopes and camera systems, which is also known as Pan-STARRS-4 (Kaiser & Pan-STARRS Team 2002). PS1 is a single telescope and camera system built to test all requirements that are needed in the full version project. PS1 telescope has an aperture of 1.8 m in diameter with 3-element wide field corrector that delivers a 7 deg^2 flat field in the focal plane. Its 8 m focal length gives a plate scale of 38.5 μm/arcsecond rendering a pixel resolution of 0.258 arcsecond/pixel. The telescope can monitor up to 240 guide stars at $\sim$ 30 Hz (in reality, probably about 60 guide stars at 30Hz with high SNR). High frequency image motion can be removed by on-chip fast guiding, where localized image motion can be calculated from a collection of nearby guide stars. Hence different image motions across the field of view can be corrected. This can only be achieved with the innovative design of an orthogonal transfer charge coupled device (OTCCD). The OTCCD allows on-chip charge shifting, in both rows and columns, which can compensate for the image motion in the focal plane (Tonry et al. 1997). The PS1 Giga-Pixel Camera (GPC1) contains an 8x8 array, minus the 4 corners, of OTCCDs. For reasons of economy of manufacture, facilitating fast readout and other practical concerns, the OTCCDs each consist of an 8x8 Orthogonal Transfer Array (OTA) of independently-addressable cells of size 590x598 pixels. Hence GPC1 comprises approximately 1.4 billion pixels. Typically, each OTA will have a single cell devoted to a guide star reading at high frequency. Of the 590x598 pixels of this cell, only a small fraction around the guide star will be read, thus allowing a fast read out with relatively low read noise.

PS1 has four filters closely resembling SDSS filters (g, r, i, z), and a y-band filter. Their pass-bands, corresponding m_1 magnitudes and sky brightness are listed in Table 1. The major sources

Table 1:: Filter bandpass, m_1 (the AB magnitude that produces 1e$^-$/sec/pixel) and average sky brightness μ in magnitudes per arcsecond at Haleakala for PS1 filters.

Filter	Bandpass (nm)	m_1 mag	μ mag/arcsec^2
g	405-550	24.90	21.90
r	552-689	25.15	20.85
i	691-815	25.00	20.15
z	815-915	24.63	19.26
y	967-1024	23.03	17.98

of noise are: shot noise, background noise from the sky, read noise, radio frequency interference and dark current noise. The SNR for a given star can be estimated by[2],

$$S/N = S/\sqrt{\sigma_{\rm P}^2 + \sigma_{\rm S}^2 + \sigma_{\rm RN}^2 + \sigma_{\rm RFI}^2 + \sigma_{\rm T}^2 + \sigma_{\rm d}^2} \quad (1)$$

where the various sources of noise are

- Poisson noise, $\sigma_{\rm P}^2 = 0.5 \times 10^{-0.4(m-m_1)} \times t$, where t is the exposure time and m is the apparent magnitude of the target star.
- (sky) background noise, $\sigma_{\rm S}^2 = \frac{\pi}{4}\omega^2 \times 10^{-0.4(\mu-m_1)} \times t$, where ω is the FWHM of the PSF in arcseconds, and μ is sky brightness in magnitude per square arcsecond;
- read noise, $\sigma_{\rm RN}^2 = \frac{\pi}{4}\omega^2 \times A \times N_{\rm read}^2$, where $A = 3.846$ pixel/arcsec^2 for 0.26 arcsecond pixels and $N_{\rm read}$ is the read noise of the detector.
- noise from radio frequency interference, $\sigma_{\rm RFI}^2 = \frac{\pi}{4}\omega^2 \times A \times N_{\rm RFI}^2$, where $N_{\rm RFI}^2$ is radio frequency interference noise.
- noise from dark current, $\sigma_{\rm d}^2 = \frac{\pi}{4}\omega^2 \times A \times d \times t$, with d counts/sec

Based on the characteristic noise mentioned above, we calculated the SNR versus magnitude with different filters under 30 Hz sampling, 27e$^-$ read-out noise, 1 arcsecond FWHM, d = 5 counts/sec and no radio frequency interference. Figure 1 shows the relation between magnitude and SNR for all filters. Except for the y filter, stars with $m_{\rm V} < 11$ mag can achieve SNR ≥ 80 with 30 Hz sampling.

[2]We took the numbers from PS1 document PSDC-230-002-00 (Mission Concept Definition http://pan-starrs.ifa.hawaii.edu/project/PSDC/PSDC-2xx/) for the characteristic noise for all possible sources.

3. Diffraction Profile of Stellar Occultation

The differential size distribution $dN/dD \propto D^{-q}$ implies that large objects are small in number. Therefore, the odds of serendipitous occultation by a large object is very small. Instead, we stand a better chance looking for occultations by objects in the small end of the size spectrum. There are two reasons for this: kilometer to sub-kilometer TNOs are far more numerous than big TNOs as the size distribution suggests, and the effective diameter of the occultation shadow is enlarged due to the diffraction effect, which effectively increases the event rates.

In diffraction theory, there are two regimes delimited by the Fresnel number $\tilde{F} = D^2/(r\lambda)$, where D is the size of the TNO, r is the distance from the object to the observer, and λ is the observing wavelength: the *Fresnel* diffraction (near field) where $\tilde{F} \gtrsim 1$ and *Fraunhofer* diffraction (far field) where $\tilde{F} \ll 1$. As we increase the size of the TNO or decrease the distance to the object, we pass from the Fraunhofer regime to the Fresnel regime. The characteristic size, known as Fresnel scale F (~ 2 km at 43 AU, 600 nm), is defined by $\sqrt{r\lambda}$ and can be used to identify the two regimes. The regime of $\tilde{F} \gg 1$ is called the *geometric* regime, however for the scope of this work the probability of having such an occultation is insignificant.

The diffraction profile of stellar occultation for a point source can be calculated by the Lommel function and the profile for stars with finite size can be obtained by convolving the point source profile with the stellar disk (Roques et al. 1987). The profile is a function of TNO distance, size and shape, stellar angular size and impact parameter (defined as the distance between the line of sight of the star and the object). Nihei et al. (2007) showed that the width of a diffraction profile H (the diameter of the first Airy ring) with zero impact parameter is defined as:

$$H(\lambda, r, D, \theta_\star) = 2\left[(\sqrt{3/2}F)^{\frac{3}{2}} + (D/2)^{\frac{3}{2}}\right]^{\frac{2}{3}} + r\,\theta_*\,, \tag{2}$$

where $\theta_\star$ is the angular size of occulted star. Figure 2 shows diffraction profiles for various TNO sizes at 43 AU with zero impact parameter at opposition. As the size of TNOs becomes smaller than the Fresnel scale, the effective diameter remains almost the same. In other words, for objects smaller than the characteristic length defined by Fresnel scale, the diffraction effect will make the effective diameter independent of the size of the object.

For non-point sources, due to the fringe superposition, stars with large stellar angular size would smear out the diffraction profile and reduce the depth of occultation as shown in Figure 3, the diffraction profiles of 600 m size TNO at 43 AU for various stellar angular sizes.

For more distant objects, the Fresnel scale gets larger, and thus the same size objects are in the Fraunhofer regime. Furthermore, the projected size of the background star gets larger, thus a distant occultation event would have longer event duration but shallower occultation depth. In Figure 4, as the distance to the objects increases, the effective diameter becomes larger, and the depth of the flux reduction gets shallower.

The diffraction profile of *spherical* objects have very distinct Poisson peak which can not be

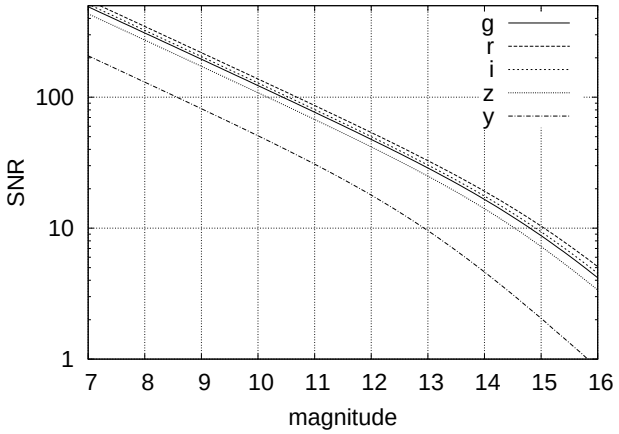

Fig. 1.—: SNR plot for PS1 filters with 27e$^-$ read out noise, 1 arcsec FWHM, $d = 5$ counts/sec and 30 Hz sampling. Sky brightness and m_1 values for each filter are taken from Table 1. Note that, except for the y filter, stars with $m_V < 11$ mag can achieve SNR ≥ 80 with 30 Hz sampling.

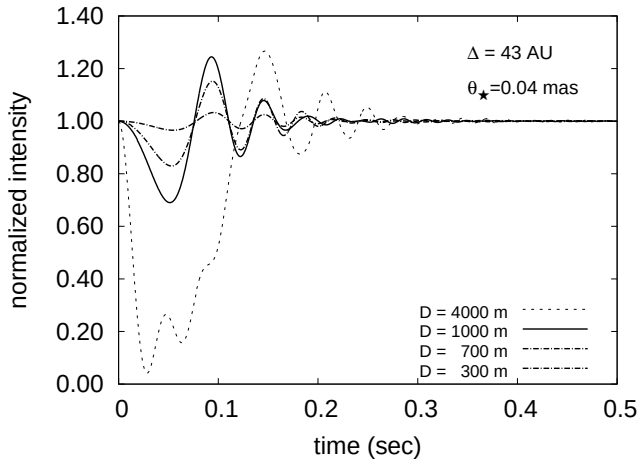

Fig. 2.—: Diffraction profiles for various TNO sizes at 43 AU and zero impact parameter at opposition. As the size of TNOs becomes smaller than the Fresnel scale, the effective diameter remains almost the same. In other words, for objects smaller than the Fresnel scale, diffraction effect will make the effective diameter larger than the geometric diameter. The Fresnel scale at 43 AU is about 2 km, therefore in this case, 300 m, 700 m and 1000 m objects all have the same effective diameter.

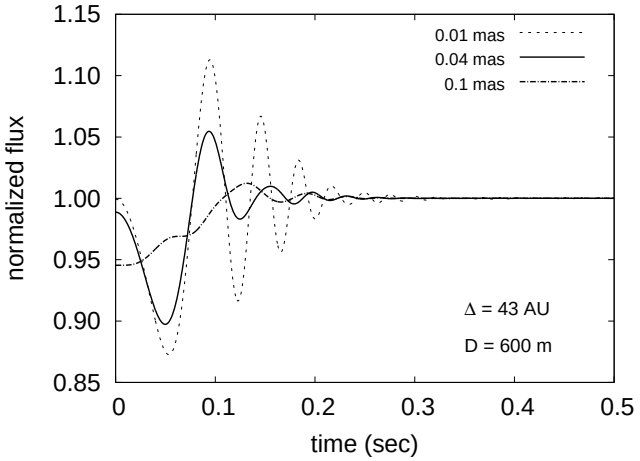

Fig. 3.—: Diffraction profiles of a 600 m size TNO at 43 AU and zero impact parameter at opposition for various stellar angular sizes. Due to the fringe superposition, a star with large stellar angular size would smear out the diffraction profile and reduce the occultation depth. As it can be seen from the differences between 0.1 and 0.01 mas stars, the diffraction profile is very distinct for 0.01 mas star and becomes shallower when the stellar angular size gets larger.

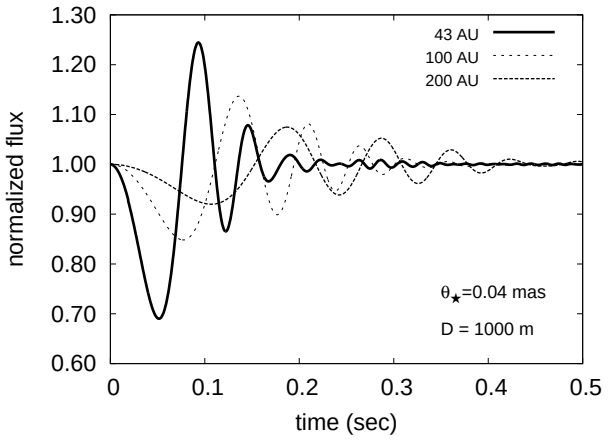

Fig. 4.—: Diffraction profile for 1 km size TNO at various distance with zero impact parameter at opposition. The effective diameter becomes larger and the depth of the flux reduction gets shallower as the distance to the TNO increases.

observed in irregular shape objects. However, as the objects become smaller than the Fresnel scale, the central Poisson peak exists for all shapes of objects (Roques et al. 1987).

Finally Figure 5 shows the diffraction pattern for various impact parameters. When the objects are smaller than the Fresnel scale, the Poisson peak is prominent for $b = 0$. The peak falls gradually, as b increases, to a trough and then the intensity reverses (brightening event) as it reaches the first Airy ring.

One can notice that in the Fraunhofer regime, for example $D = 500$ m at 43 AU, the shape and size do not change the width of the diffraction profile, only the depth of the occultation is affected by the object size and impact parameters. We based our detection method on this property as we explain in the following section.

4. Detection Method

When the shadow of a stellar occultation sweeps across a telescope, high sampling rate systems like PS1 video mode will translate the shadow with diffraction profile into several time-sampled lightcurve points. In order to look for signatures of occultation, a detection method should be able to probe these lightcurves for diffraction patterns. There are far more numerous TNOs smaller than the Fresnel scale, therefore we target our search at objects with $D \leq F$. In this regime, H does not change as a function of the object size, shape or stellar spectral type. On the other hand, the depth of the occultation depends on the object size and stellar angular size. Also, the shape of the diffraction profile depends on the impact parameter.

Based on these conditions, we have designed our detection method to search for occultations by scaling pre-defined TNO diffraction profiles (i.e. templates) to match patterns in the lightcurves. For a given star, with known stellar angular size $\theta_\star$ and SNR S, let $g(\tau; b, \{\theta_\star, S\})$ be a normalized template with mean zero as a function of time τ and impact parameter b. We then try to find the best matched template by maximizing the following measure,

$$\mathcal{M}(\tau) = \sum_{\tau=t-w}^{\tau=t+w} \left[\alpha\, g(\tau; b, \{\theta_\star, S\}) - p(\tau)\right]^2 \ , \tag{3}$$

with respect to the scaling factor α, where p is the local nominal baseline subtracted lightcurve within a window $[-w : +w]$. The size of the window n can be found analytically as $sH/v_{\rm rel}$, where s is the sampling rate, $v_{\rm rel} = v_{\rm e}\,(\cos\phi - \sqrt{r_{\rm AU}^{-1}})$ is the relative velocity with v_e is the orbital speed of the Earth, ϕ is the opposition angle and $r_{\rm AU}$ is the distance of a TNO to the observer in units of AU. Finding the scaling parameter α can be done analytically as:

$$\alpha(b, \{\theta_\star, S\}) = \frac{\sum p(\tau)\, g(\tau; b, \{\theta_\star, S\})}{\sum g(\tau; b, \{\theta_\star, S\})^2} \, . \tag{4}$$

To consider the effect of b, we simply maximize α over b,

$$\tilde{\alpha}(\{\theta_\star, S\}) = \max_b \left[\alpha(b, \{\theta_\star, S\})\right] \ . \tag{5}$$

In practice, for a given $\theta_\star$ and S, we built a set of templates with impact parameter values, $b = \{0.00H, 0.01H, 0.02H, \ldots, 0.50H\}$, and scan all templates across the lightcurve to find the template that maximizes $\alpha(b, \{\theta_\star, S\})$. In order to speed up the computation, we actually perform a two-pass procedure. The first pass involves scanning corresponding templates from $b = 0.0H$ to $0.5H$ with $\Delta b = 0.1H$ to find the region that brackets the maximum α. Then within this region, we apply a second pass that uses templates with finer impact parameter step, $\Delta b = 0.01H$, and again find the maximum α value within this region. The template that gives the largest α value is the best fit between the scaled template and a pattern in the lightcurve. At the end of this process, we have the same number of optimized α's as the number of points in all lightcurves[3]. In order to decide if any of these α values represent real events or false positives, we determined a threshold value $\alpha_{\rm t}(\theta_\star, S)$, calculated from the *null* hypothesis distribution. For this purpose, we simulated lightcurves with no events, then scanned templates through these lightcurves, optimized for α's, built the distribution, set the p-value based on the desired false positives and finally determined the $\alpha_{\rm t}(\theta_\star, S)$ accordingly.

This distribution can also be estimated semi-analytically, thereby reducing the computational cost. Finding an optimized parameter using a least square metric while minimizing over another parameter is equivalent to a regression with one nuisance parameter (Rice 2007). The cumulative distribution of such a system is known to follow the *Gumbel distribution* or type I *extreme value distribution* (Gumbel 1943),

$$G(X \leq x) = e^{-e^{-\nu(x-\mu)}} \ , \tag{6}$$

where ν and μ are fitted parameters (scale and location parameters).

The left panel of Figure 6 compares the null hypothesis cumulative distribution of $\tilde{\alpha}$'s, for SNR=100 and $\theta_\star = 0.01$ mas, built from simulations (solid points) with the fitted Gumbel distribution (solid line). As can be seen from the figure, the fitting for cumulative distribution < 0.8 ($\tilde{\alpha} < 0.2$) was good. But the fitted part of the tail ($\tilde{\alpha} > 0.2$) of the distribution, which is the part we care about the most, did not fit well. Therefore, we separately fitted the tail part of the cumulative distribution, and the results are shown in the inset of left panel of the same figure. Note that the difference in the tail between the null hypothesis distribution and the fitted Gumbel distribution is now very small. The right panel of Figure 6 shows the number of false positives predicted by Gumbel distribution versus the number of false positives observed in the simulation. As can be seen, at high threshold (bottom-left corner) the number of predicted false positives is more than the number of observed false positives. This is due to the fact that the $\alpha_{\rm t}(\theta_\star, S)$ set by fitted Gumbel distribution is actually higher than that of the true null hypothesis distribution. As

[3]There are actually fewer $\tilde{\alpha}$'s than number of points because at the beginning and end of the lightcurves there are not enough points to define the local nominal baseline.

a result, even though the threshold will be set a bit higher, $\alpha_{\rm t}(\theta_\star, S)$ can be still calculated based on the Gumbel distribution to ensure one false positive in the lifetime of the project. In reality, we may get fewer than one false positive, as we demonstrated above.

The next step is to search in the lightcurves for any $\tilde{\alpha}$ values that are larger than the $\alpha_{\rm t}(\theta_\star, S)$. Note that the $\alpha_{\rm t}(\theta_\star, S)$ is $\theta_\star$ and S dependent, thus the process of simulating the null hypothesis distribution and fitting for ν and μ has to be repeated for each individual star. In order to alleviate this problem, we have constructed a grid of fitted $\alpha_{\rm t}(\theta_\star, S)$'s values for various SNRs and angular sizes a priory and tabulated these values into a database. For a given star, the threshold is approximated with $\alpha_{\rm t}(\theta'_\star, S')$ where $\theta'_\star$ and S' are the closest pre-calculated values to $\theta_\star$ and S.

Note that in the presence of auto-correlations (trends) in the lightcurves the Gumbel distribution may not best describe the data. We have not yet investigated how well this approximation performs when trend exists in the lightcurves. Therefore, in the event detection pipeline, we apply a high-pass filter and de-trend the lightcurves to avoid this difficulty (see §8).

To estimate the detection efficiency as a function of TNO-size for PS1 guide stars with various SNRs and angular sizes, we implanted objects with various sizes into simulated lightcurves and calculated the number of $\tilde{\alpha}$ values for each object size that are larger than the threshold value $\alpha_{\rm t}(\theta_\star, S)$. Figure 7 left panel shows the detection efficiency for different stellar angular sizes as a function of object size. As the plot suggests, PS1 can detect objects as small as ~ 400 m. Figure 7 right panel shows the detection efficiency as a function of SNR and $\theta_\star$ for 700 m obejcts; the detection efficiency is higher for higher SNRs and smaller stellar angular sizes. Therefore the guide stars selection (see §7) should be based on this fact: stars with higher SNR and smaller stellar angular size are best candidates for searching stellar occultation in the lightcurves.

To evaluate whether our detection process is computational feasible, we have estimated the total float point operations (FLOP) needed to process all data for one night to be $\sim 10^{11}$ (this is a conservative estimate). To save computational time, we firstly tabulate the values of $\sum g(\tau; b, \{\theta_\star, S\})^2$ in Equation 4. The two-pass procedure to search for matched template needs about 25 FLOP. Each template has 13 data points, therefore for each data point in the lightcurve, the computational cost is about 325 FLOPS and for each night, there will be a total of $\sim 5 \times 10^7$ data points assuming 30Hz sampling and 60 guide stars. With a 3G Hz CPU, the whole detection process can be done in few minutes.

Bickerton et al. (2008) has demonstrated a similar detection method using convolution of templates with lightcurves. The advantage of convolution done in Fourier space is that it is computationally faster. Nevertheless, our computational cost is not significant as we have pointed out above, and therefore we choose to do the template matching in real space in order to avoid problems of aliasing and for better control and understanding of the underlying distribution.

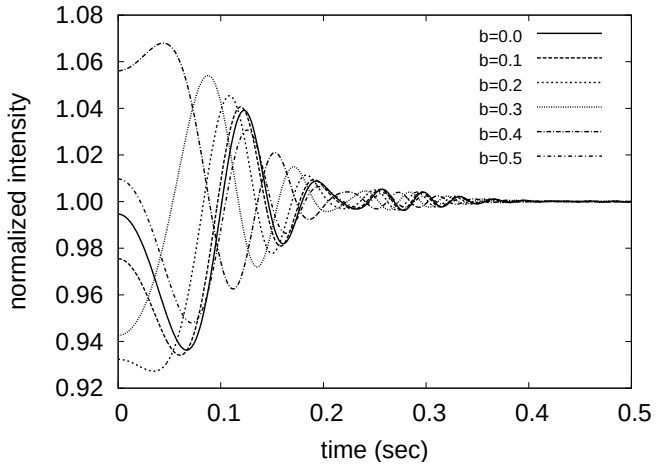

Fig. 5.—: Diffraction profile for 500 m size TNO at 43 AU with various impact parameters at opposition. The central Poisson peak drops as the impact parameter increases until it reaches the first Airy ring where the intensity goes up again.

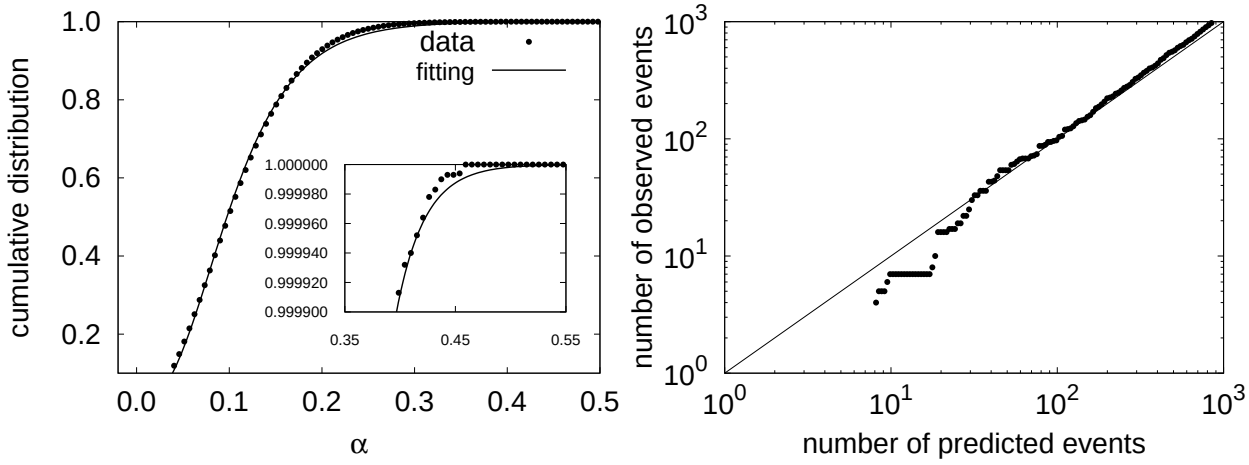

Fig. 6.—: Left panel shows the null hypothesis distribution of α values (shown for SNR=100 $\theta_\star = 0.01$ mas with dots) and fitted Gumbel distribution (solid line). From a separate fitting to the tail part (inset), the difference between the null hypothesis distribution from simulation and the fitted Gumbel distribution is very small. The right panel shows the number of false positives predicted by Gumbel distribution versus the number of false positives observed in the simulation. The diagonal line is to show the difference between predicted and observed values. As can be seen that at high threshold (bottom-left corner), the number of predicted false positives is more than the number of observed false positives.

5. Estimate of The Stellar Angular Size

As mentioned before, the stellar angular size is important in choosing the guide stars. For this reason we need to be able to estimate these angular sizes ahead of time in order to select guide stars that will yield the highest number of events.

Various methods have been used to measure stellar angular sizes -for example, lunar occultation, stellar interferometry, speckle interferometry, and other photometric and spectrophotometric methods (see Scholz (1997) and reference therein). However, these measurements from the literatures are limited to relatively few bright stars. An alternative way to select the most appropriate guide stars from all stars visible to PS1 3π sky, is to estimate the stellar angular sizes using their colors. For example, Van Belle (1999) fitted a few stars with known zero magnitude angular sizes ($\theta_{V=0}$ and $\theta_{B=0}$) versus their $(V-K)$ and $(B-K)$ colors to set up the relation between the color indices and their angular sizes. Accordingly, we used the formulae in his work in combination with the Tycho2 [4] catalog (Høg et al. 2000) for V-band magnitudes, and the 2MASS [5] catalog (Skrutskie et al. 2006) for K-band magnitudes. We first extracted all stars with $m_{\rm V} < 13$ mag and $m_{\rm K} < 16$ mag above the PS1 southern declination limit $\delta \geq -30^{\circ}$ and cross matched stars from each catalog by looking for pairs within one arcsecond radius and calculated their corresponding $(V-K)$ color. We then refitted recent measurements of angular sizes from the Catalog of Apparent Diameter and Absolute Radii of Stars (CADARS) compiled by Pasinetti Fracassini et al. (2001) with Van Belle (1999)'s relations. We obtained the following fitted relation:

$$\theta = 10^{[0.453\pm0.003+0.246\pm0.005(V-K)-0.2V]}\,, \tag{7}$$

for main sequence stars and

$$\theta = 10^{[0.407\pm0.007+0.238\pm0.009(V-K)-0.2V]}\,, \tag{8}$$

for giants. The fitting results are shown in Figure 8 and as can be seen, the predicted values matched well with the measured ones for both main sequence and giant stars.

Due to the fact that stellar angular sizes depend not only on the spectral type but also on the luminosity class, the next question is how to reckon the luminosity class for every matched star when there is no such information. To do so we relied on the $(V-K)$ color as a way to (roughly) distinguish between main sequence and giant stars. On the left panel of Figure 9 we show that the distribution of $(V-K)$ from all matched stars in PS1 3π sky has two peaks, suggesting two groups of stars - most likely main sequence and giants. We used the luminosity class information provided in CADARS to determine the boundaries between these two classes (shown in Figure 9 middle panel). Based on this, all stars with $(V-K) \leq 1.85$ were considered to be the main sequence stars and all stars with $(V-K) > 2.0$ to be giants. We abstained from classification for stars

[4] http://archive.eso.org/ASTROM/TYC-2/readme.htm

[5] http://www.ipac.caltech.edu/2mass/

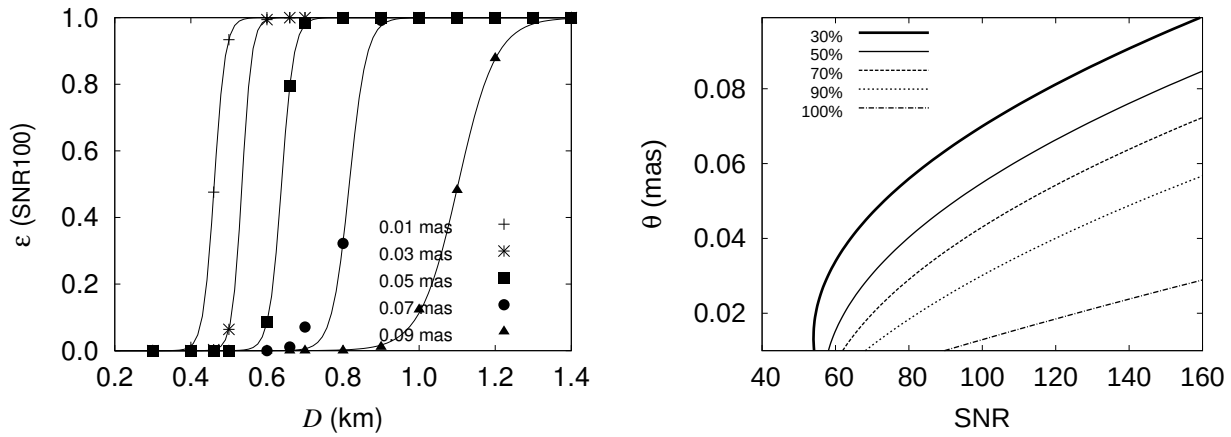

Fig. 7.—: The left panel is the efficiency as a function of TNO size for SNR=100 and various stellar angular sizes. The right panel is the efficiency contour as function of SNR and stellar angular size for 700 m objects. Stars with higher SNR and smaller stellar angular size have higher detection efficiency and are best candidates for searching stellar occultation in the lightcurves.

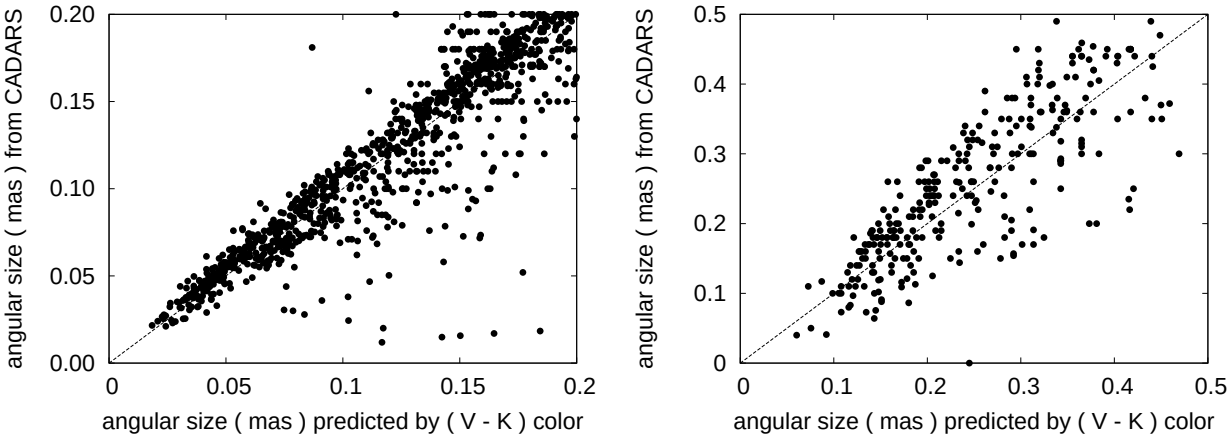

Fig. 8.—: Angular sizes predicted from Equation 7 and Equation 8. The predicted values matched well with both main sequence (left panel) and giant (right panel) stars from CADARS.

between these boundaries. Note there are still a few giant stars with small $(V-K)$ (see middle panel of Figure 9). This is a selection bias in the catalog due to the fact that these are bright blue O or B giant stars with multiple measurements. In reality, O and B giant stars are rare and can be removed from the final catalog using known O and B star catalogs (Reed 2003; Maíz-Apellániz et al. 2004).

Using the $(V-K)$ cut, Equation 7 and Equation 8, we predicted angular size for CADARS stars and estimated the rms error to be 21.7% for main sequence and 20.6% for giants.

Finally we estimated the angular sizes for all matched stars visible to PS1 3π sky and the resulting distributions are shown in Figure 9 (right panel). Main sequence stars peak around 0.02 mas, and giants peak around 0.05 mas where the overall distribution (solid-line) peaks around 0.02 mas.

6. Event Rate Based on Various Models

In this section we estimate the number of expected events for the three year project lifetime based on different models. The comparison of the number of expected events with the actual observed events will allow for discrimination between the different models.

One can estimate the number of expected events as a combination the total solid angle, detection efficiency and differential size distribution. It follows that:

$$\mathcal{N}_{\rm event} \simeq \sum_{k}^{n}\sum_{j_k}^{n_{j_k}} v(\phi_{j_k},r)\ \xi_{j_k}\ \frac{1}{r^2}\int_0^\infty \frac{dN}{dD}\times H\left(\lambda,r,D,\theta_k\right)\ \epsilon(\lambda,D,\theta_k,S_k)\,dD\ , \tag{9}$$

where n is total number of guide stars, j_k is the jth exposure for guide star k, $v(\phi_{j_k},r)$ is the apparent motion of the TNO for guide star k and exposure j_k, ξ_{j_k} is the exposure time, dN/dD is the differential size distribution, $H(\lambda,r,D,\theta_k)$ is the effective diameter, and $\epsilon(\lambda,D,\theta_k,S_k)$ is the detection efficiency for PS1. The apparent motion $v(\phi_{j_k},r)$ and effective diameter $H_k(\lambda,r,D,\theta_k)$ can be calculated with $\phi=0^\circ$ (PS1 will observe mainly close to opposition) for all stars and all pointings, $r=43$ AU and λ's corresponding to the particular filters. The total number of exposures n_{j_k} for each star k will be *reduced* according to the time that PS1 is pointing within the ecliptic. If we assume that TNOs are distributed uniformly within $|\beta|\leq 6^\circ$ along ecliptic, the total time PS1 will spend near ecliptic is then $\sin(\beta)\,\tau\simeq 0.10\,\tau$, where τ is the total time of observation in seconds for a three-year lifetime. The detection efficiency for PS1 has been investigated as a function of θ_k and S_k in §4. The last unknown in the event rate calculation is the model dependent differential size distribution. For this, we adapted three differential size distributions. First, we used a double power-law distribution described in Bernstein et al. (2004) (hereafter B04) with bright-end slope $\alpha_1=0.88$ and faint-end slope $\alpha_2=0.32$. The conversion from R-magnitude to size of the TNO was done by using 4% albedo and $\phi\sim 0^\circ$ (Russell 1916). The cumulative size distribution is shown as B04 line in Figure 10. Second, we use the models by Pan & Sari (2005) (hereafter P&S05)

with three different break diameters at 20, 40 and 80 km and $q = 3$ also shown in Figure 10. The third model is from the upper limit set by the TAOS project (Zhang et al. 2008) (hereafter Z08). Anchored at 28 km, TAOS collaboration reported an upper limit on the cumulative surface density for objects larger than 0.5 km shown as solid circle (anchored point) and solid square (upper limit) also in Figure 10. Other models, such as Kenyon & Bromley (2004), predicted the cumulative size distributions for sub-kilometer objects to be within the ranges of the three models mentioned above and hence are not shown here.

We next calculate the number of events for three models assuming 300 clear nights per year, eight hours of observation per night and 60 guide stars with 0.02 mas and SNR=100 for PS1 three-year lifetime as show in Figure 11. From the TAOS upper limit, the most optimistic prediction for the number of events is ∼100. The P&S05 model with different break diameter have number of events ranging from a few to a few tens. For B04, we expect less than one event in PS1's three year life-time.

7. Guide Stars Catalog

As we have shown in the previous section, the detection efficiency is higher for smaller stellar angular size and higher SNR. Therefore, it is crucial to select guide stars with the smallest possible angular size yet with good SNR in order to maximize the detection rates. Nevertheless, it is not clear whether a star with SNR=120, $\theta_\star$=0.07 mas is a better choice than another star with SNR=100 and $\theta_\star$=0.03 mas. To answer this question we chose a size distribution from models, such as P&S05 with break diameter $D_\mathrm{b} = 40$ km, and calculated the number of expected events for a given star. In Figure 12, we show the total number of expected events per star in PS1's three-year lifetime as a function of angular size and SNR. Using this relation, we can now estimate the event rates for all matched stars (i.e., candidate guide stars) from Tycho2 and 2MASS catalogs and then select stars that give the highest event rates as our guide stars.

In Figure 13, we show the distribution of $m_\mathrm{V} < 13$ mag for all Tycho2 stars visible to PS1 3π sky along with all matched stars between Tycho2 and 2MASS catalogs. For this work, we removed all matched stars with $m_\mathrm{V} < 8.5$ mag due to possible saturation. As it can be seen, most of the stars with $m_\mathrm{V} < 12$ mag were matched. On average, there are about 180 candidates with $m_\mathrm{V} < 11.5$ mag for every PS1 7 deg^2 field. Furthermore, Figure 12 shows the number distribution of matched stars as a function of SNR and $\theta_\star$. The distribution of SNR peaks around 80 and the angular size peaks around 0.02 mas.

Considering that only 60 guide stars are needed for each target field, we selected $\sim 3\times10^5$ guide stars from a total of $\sim 1.27\times10^6$ candidates [6,7]. The dotted line in Figure 13 is the distribution of

[6]For 3 π sky and PS1 7 deg^2 field of view there are about 5000 unique target fields.

[7]We have compiled a complete list for all matched stars with $m_v < 13$ mag. For the complete list see

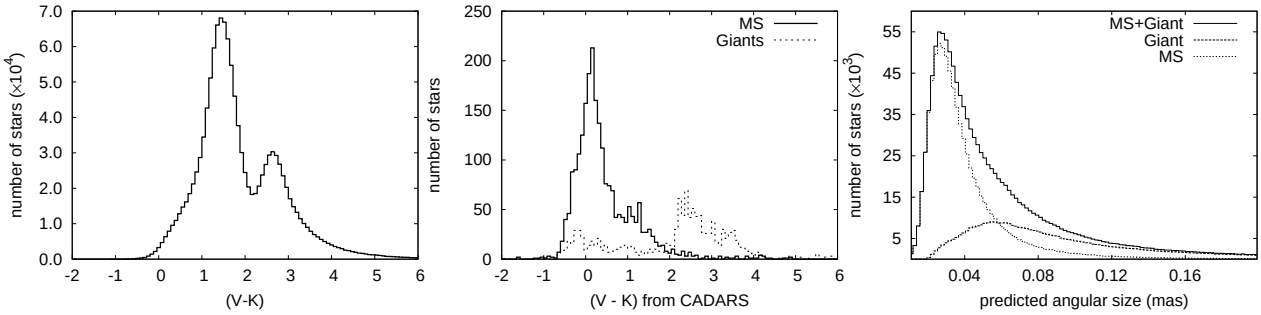

Fig. 9.—: Left panel: Distribution of $(V-K)$ of all matched stars between Tycho2 and 2MASS catalogs. As it can be seen, there are two peaks in the distribution, indicating contribution from main sequence (left peak) and giant (right peak). Middle panel: The $(V-K)$ distribution of the measurements from CADARS. The number of main sequence stars dropped quickly for $(V-K) > 2.0$ and so is the number of giants for $(V-K) < 2.0$. Right panel: The distribution of predicted angular size of the matched stars between Tycho2 and 2MASS. Main sequence stars peak around 0.02 mas, and giants peak around 0.05 mas. The overall distribution (solid-line) peaks around 0.02 mas.

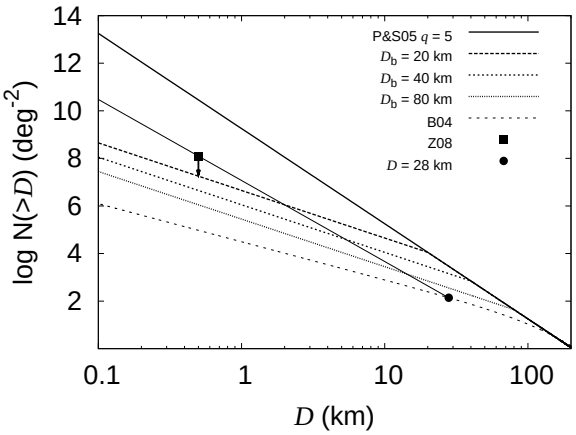

Fig. 10.—: The straight solid line (P&S05) has $q = 5$. The slope after the break diameter has $q = 3$. Double power law from Bernstein has $\alpha 1 = 0.88$ and $\alpha 2 = 0.32$ (B04). TAOS (Z08) upper limit was anchored at 28 km on the B04 model and set an upper limit with $q < 4.6$ at 0.5 km. The arrow indicates an upper limit.

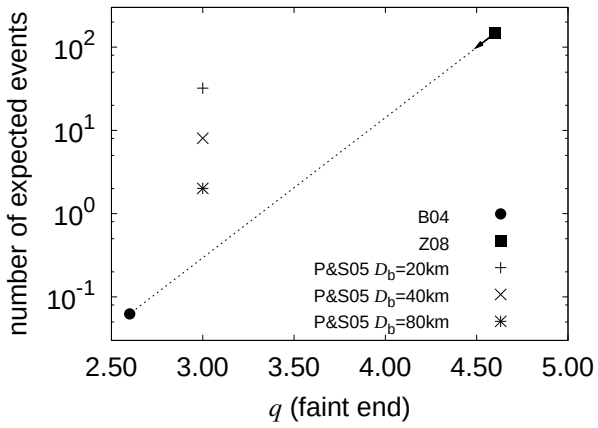

Fig. 11.—: Total number of expected events in the PS1 three-year lifetime, assuming all 60 guide stars are 0.02 mas and SNR=100, for different models. The arrow between Z08 and B04 indicates that the number of expected events will move along the dash-line as the upper limit (i.e. q) becomes smaller (as stronger constraints apply to the upper limit). Number of expected events from Z08 gives the most optimistic value of ~ 100. The number of expected events from P&S05's models range from a few to a few tens. For B04, we expect less than one event in the PS1 three-year lifetime.

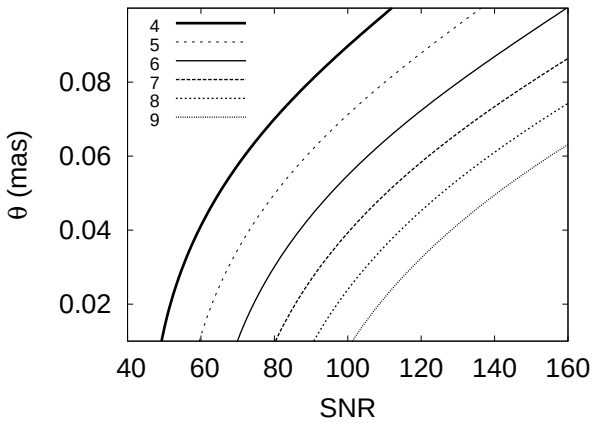

Fig. 12.—: Total number of expected events in the PS1 three-year lifetime. Given SNR, $\theta_\star$ and Pan & Sari's model with 40 km break diameter with $q = 3$, assuming all 60 guide stars have the same angular sizes and SNRs.

the top 3×10^5 stars that were selected for the highest event rates. It is clear that most of these stars are also bright ($m_{\rm V} < 11.2$ mag). In reality, even if the guide stars were selected based solely on their SNR, only a few stars per field would have not been selected from our selection based on the event rates. For each PS1 target field, we provide multiple choices of guide stars ranked by the estimated event rates. Multiple choices will ensure freedom of selecting guide stars away from gaps in CCD arrays or dead pixels that would develop over time.

8. Engineering Data

A set of video mode engineering data ($\sim$ 166 stars-hours) was acquired in fall of 2008. The guide stars used in these images were randomly picked bright stars as opposed to being selected based on the optimized event rates as we described in previous section. Each FITS (Wells et al. 1981) cube in the data set contains a few thousand 100×50 pixels images with one bright guide star. For the purpose of testing, these images were taken with 10 Hz instead of 30 Hz sampling. Nevertheless, we calculated all the related threshold values for 10 Hz sampling and tried to look for possible events in these engineering data.

All images in the FITS cube were processed with *SExtractor* (Bertin & Arnouts 1996) to extract lightcurves for every guide star. Lightcurves for stars on the edges were excluded, and the first and last 100 data points in the lightcurves were removed because no stars were in these images due to shutter operations.

We applied high-pass filter to the lightcurves to remove the low frequency components (calculated by a running mean from 21 data points) and then de-trending to remove the common features existing among the lightcurves taken at the same time (Kim et al. 2009). Figure 15 shows two examples of lightcurves along with their autocorrelations before and after the lightcurves were high-pass filtered and de-trended. The raw lightcurves showed considerable fluctuations due to either changing sky transparency or image motion, resulting in significantly lower measured SNR than predicted SNR from Equation 1. Measured SNR here is the median value divided by the standard deviation of the lightcurve. Also, strong autocorrelations were present in the raw lightcurves, which can compromise the detection technique. Nevertheless, the filtered and de-trended lightcurves show improved SNR and low autocorrelations. Dashed lines in the right panels are the two-sigma range for autocorrelation of white noise: $(z - l)/z\,(z + 2)$, where z is the number of data points in the lightcurve and l is the lag in the autocorrelation (Box & Pierce 1970).

Finally we searched for possible events using the detection algorithm described in §4. To determine if the performance of detection method on the engineering data is consistent with the simulations. One of the guide star ($\alpha = 333.4820917°$, $\delta = 1.2981389°$) lightcurves with $\theta_\star \sim 0.04$ mas and $m_{\rm V} = 11.12$ mag and measured SNR = 76.3 was selected and events with various

---

http://timemachine.iic.harvard.edu/andrew/ps.matched.all.uniq

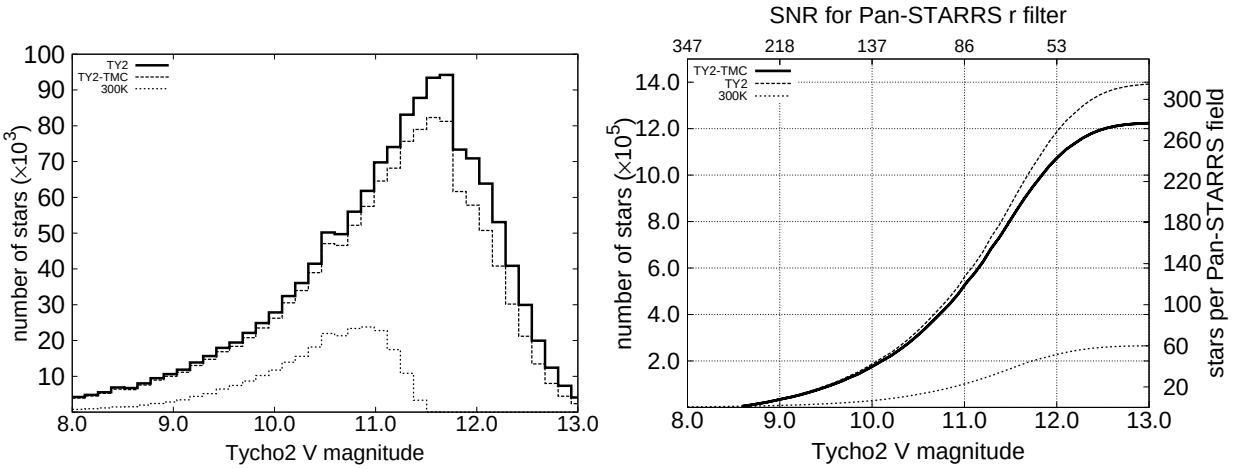

Fig. 13.—: The left panel: Histograms of all stars visible to PS1 3π sky in Tycho2 catalog with $m_{\rm V} < 13$ mag (TY2), cross-matched stars between Tycho2 and 2MASS (TY2-TMC) and the top 300 thousands cross-matched stars (300K) that give the highest event rates based on their predicted angular sizes, SNRs and P&S05 model. The peak distribution is near $m_{\rm V} \sim 10.8$ mag which has predicted SNR ~ 100. The right panel: Cumulative distribution. On average, there are 180 stars with $m_{\rm V} < 11.5$ mag for each PS1 7 deg^2 field; hence we can have multiple choices of guide stars ranked by their predicted event rates.

sizes were injected. The detection method was then used to recover the injected events and therefore the efficiency (see Figure 14). Compared with the efficiency of 30 Hz for the similar SNR and $\theta_\star$, one can see the detection efficiency of 30 Hz is better than that of 10 Hz. This also confirms that higher sampling rate has better detection efficiency. Meanwhile, the efficiency from the simulation for similar SNR and $\theta_\star$ was slightly better than the video mode lightcurve as expected.

To further evaluate the quality of the lightcurves, we compared the predicted SNR with the SNR of lightcurves before and after filtering and de-trending (see left panel of Figure 16). As it can be seen in the plot, the measured SNR is never as good as the predicted ones. In fact, the SNR of the lightcurves of bright guide stars never exceed ~ 200, which suggests that the SNR is limited by scintillation noise (Young 1967; Gilliland & Brown 1992). The scintillation noise is estimated by Equation 11 in Gilliland & Brown (1992):

$$\mathrm{SNR}^{-1} = 0.09 A^{-2/3} (\chi)^{1.75} \exp(-h/h_0)(2\Delta t)^{-1/2}, \tag{10}$$

where A is the diameter of the telescope in centimeters, χ is the air mass, $h = 3000$ m is the altitude at Haleakala, $h_0 = 8000$ m is the scale height and Δt is the exposure time in seconds. The scintillation limit based on PS1 parameters are shown as dotted line in the right panel of Figure 16. The engineering data has SNR < 200 which is consistent with the scintillation noise with PS1 parameters. The immediate impact of the reduction in the measured SNRs is the number of expected events.

In Figure 11, we estimated the event rates from the distribution peak of predicted SNR(=100) and $\theta_\star = 0.02$ mas of the guide stars candidates. If the distribution peak of measured SNRs is reduced from 100 to 50, then the number of expected events will be halved (estimated from SNR $=$ 50, $\theta_\star = 0.02$ mas in Figure 12). Nevertheless, given the wide range of expected events depending on the models and other assumptions, we are still able to impose constraints and eliminate models.

We realized that these engineering data might not be taken from the best sky condition with optimal optical and mechanical performances. Significant discrepancy can be seen between the measured SNR and scintillation noise limit (Figure 16). Possible sources of the noise are image motion, defocusing and other unknown electronic noise. We expect the quality of the video mode images will be improved in the future, and better SNRs can be achieved as of optical and mechanical problems are solved. In the end, no event in the engineering data set passed the one false positive threshold as was expected from our event rate calculations.

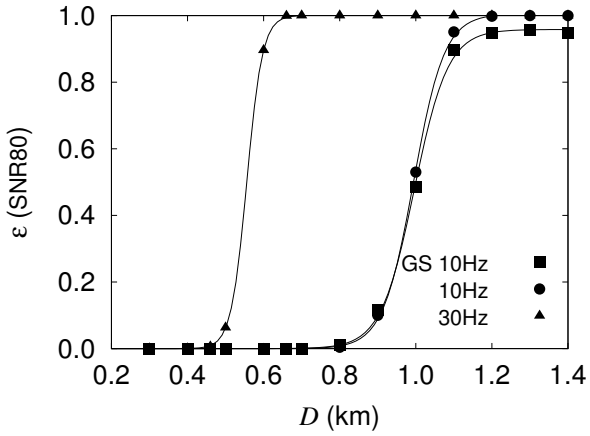

Fig. 14.—: The detection efficiency of a guide star in the 10 Hz engineering data (solid square) with $\theta_\star \sim 0.04$ mas, SNR $\sim$ 76.3. Events with various sizes were injected in the lightcurve to check the detection efficiency. Compared the detection efficiency of 30 Hz, it is clear that higher sampling rate has better detection efficiency. Meanwhile, the efficiency from the 10 Hz simulation (solid circle) for similar SNR and $\theta_\star$ was slightly better than the video mode lightcurve as expected. Most importantly, it also confirms that our detection algorithm works for PS1 lightcurve and can be used to search for TNO occultations.

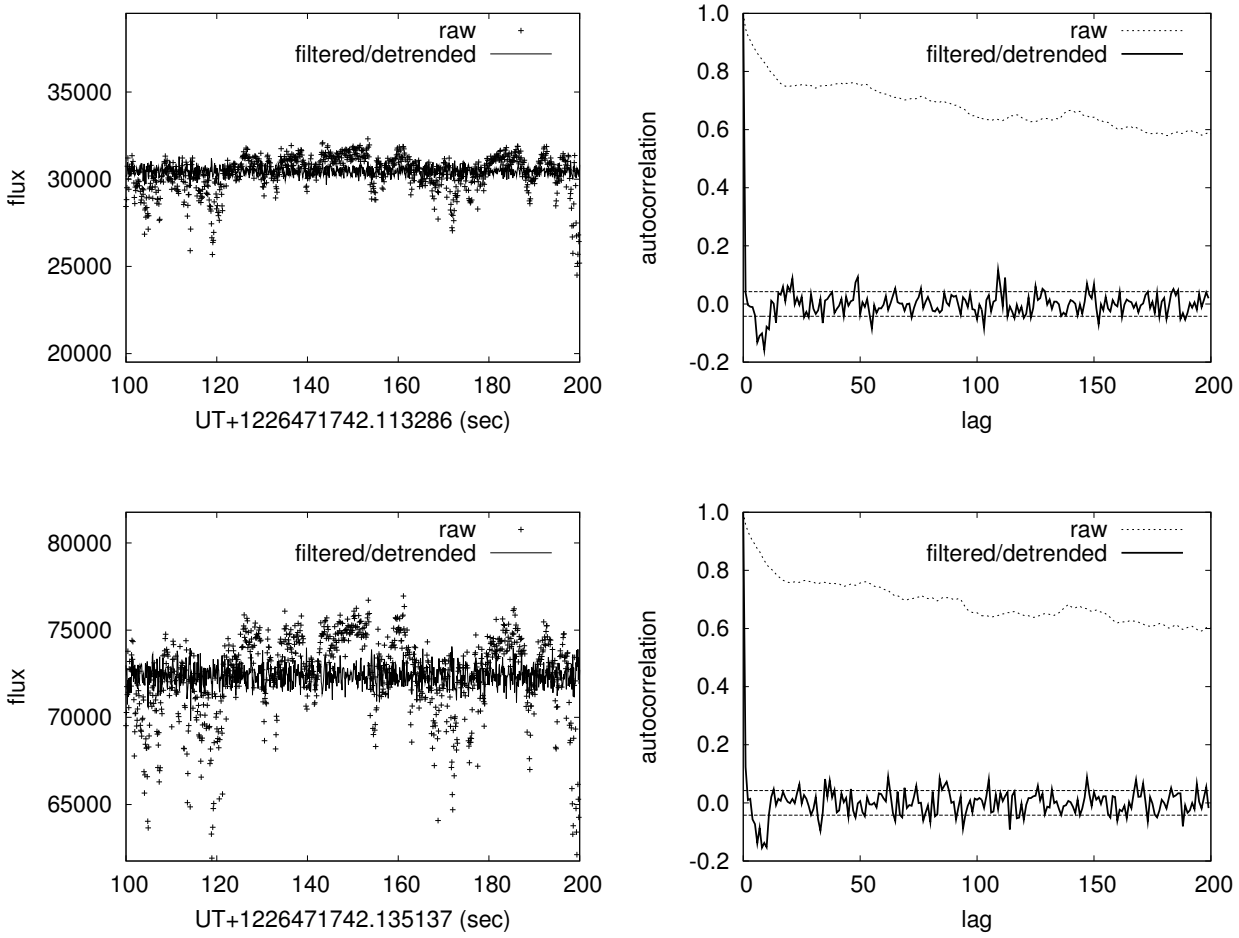

Fig. 15.—: These two lightcurves and their autocorrelations are from the same video mode batch. Left panel: The crosses are the raw lightcurves and the solid lines are the high-pass filtered and de-trended ones. High-pass filtering was done by removing a running mean of neighboring 21 data points from the lightcurves. Right panel: The autocorrelations of the lightcurves before and after processing. The dashed lines are the two-sigma range for autocorrelation of white noise (Box & Pierce 1970). As it can be seen, high-pass filtering and de-tredning improved the SNR of the lightcurves and also removed the correlation from the lightcurves.

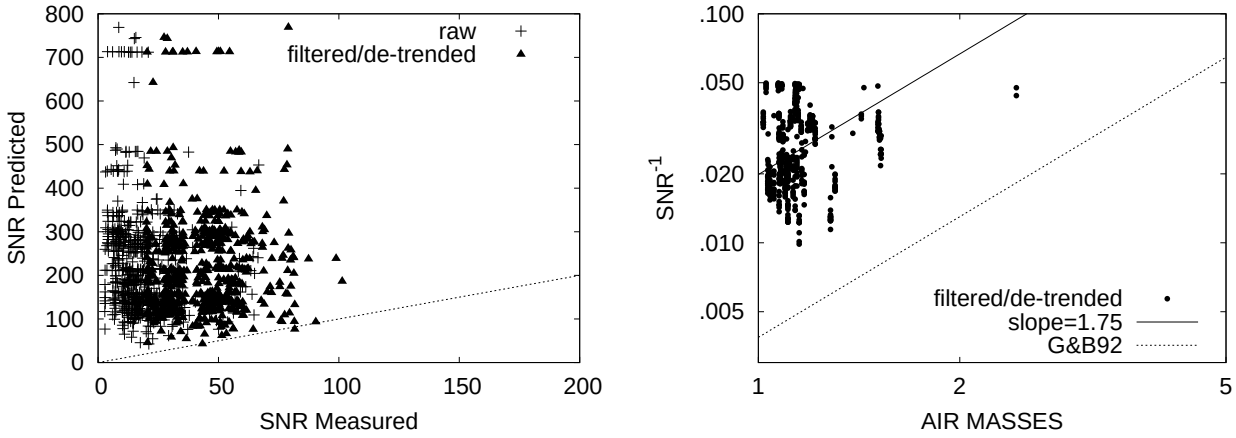

Fig. 16.—: Left panel: The predicted SNR versus the measured SNR before and after filtering and de-trending. The dotted line has slope = 1 to guide the eye. Even after filtering and de-trending, most of the measured SNRs were worse than the predicted ones. Right panel: The air masses versus the SNR^{-1}. G&B92 is the scintillation noise limit described by Gilliland & Brown (1992). The solid line is a fitting with fixed slope = 1.75 of all measured SNR. The significant discrepancy suggests that other sources of noise, such as image motion, defocusing and unknown electronic noise, also contributed to the measured SNR.

9. Result and Discussion

We have made a pre-survey study of using lightcurves from guide star video mode images to search for occultation by TNOs near 43 AU. Simulations were made to calculate the null hypothesis distribution (Figure 6) and detection efficiency for various angular sizes and SNRs. Under 30 Hz sampling, PS1 can detect objects as small as $\sim$ 400 m at 43 AU (Figure 7). Using $(V - K)$ indices, we predicted the angular sizes of all matched stars between Tycho2 and 2MASS catalogs with $m_{\rm V} < 13$ mag and $m_{\rm K} < 16$ mag above the PS1 southern declination limit $\delta \geq -30^{\circ}$. The distribution of stellar angular sizes peak around 0.02 mas in PS1 3π sky (Figure 9). On average, there are about 180 stars with $m_{\rm V} < 11.5$ mag for PS1 7 deg^2 field of view. Given that we can choose only 60 guide stars for each PS1 target field, we ranked our guide star candidates by their number of expected events based on their angular sizes, SNRs and model by P&S05. As mentioned before, multiple choices of guide star will ensure us the freedom of selecting guide stars away from gaps in the CCD array or dead pixels that would develop over time. Based on the differential size distribution from different models and the threshold to have one false positive in the PS1 three-year lifetime, we estimated the number of expected events could be somewhere from 1 to $\sim$ 100 (Figure 11). The engineering data allowed us to investigate the quality of the lightcurve and develop the detection pipeline for the upcoming real data. We have established that the detection technique performs as well with the filtered engineering data. We also realize that the true SNR is limited by systematics. Some of the systematics will be removed as we move to real data stream, however some of the systematics will remain. For example, scintillation will limit the SNR to about 200. We have recalculated the event rates with the worst case scenario and found that the event rates were compromised by a factor of four. Even with this pessimistic estimation the event rate that PS1 will find can allow us to place a constraint on the size distribution and hence the evolution of the TNOs. Using the available engineering data and detection efficiency at 0.4 and 0.5 km, we were able to derive an effective solid angle $\sim 2.3 \times 10^{-11}$ and $\sim 1.2 \times 10^{-10}$ deg^2 and set the 95% confidence upper limit on surface number density at $N(> 0.4\,{\rm km}) \sim 1.3 \times 10^{11}$ and $N(> 0.5\,{\rm km}) \sim 2.47 \times 10^{10}$ deg^{-2} (Figure 17). In future work, for the upcoming real data, we will set the threshold based on maximum true positive to false positive ratio, which allows more candidate events for further investigations. Meanwhile, the video mode lightcurves can also be used to search for objects in Sedna like orbits from 100 to 1000 AU. We will work on a new detection algorithm that is capable of searching for objects in this region.

Work at NCU was supported by the grant NSC 96-2112-M-008-024-MY3. Work at the CfA was supported in part by the NSF under grant AST-0501681 and by NASA under grant NNG04G113G. Work at ASIAA was supported in part by the thematic research program AS-88-TP-A02. And we also like to thanks IIC for hosting J-H Wang for his staying.

REFERENCES

Allen, R. L., Bernstein, G. M., & Malhotra, R. 2001, ApJL, 549, L241

Bailey, M. E. 1976, Nature, 259, 290

Bernstein, G. M., et al. 2004, AJ, 128, 1364

Bertin, E., & Arnouts, S. 1996, 117, 393

Bianco, F. B., et al. 2009, ArXiv e-prints

Bickerton, S. J., Kavelaars, J. J., & Welch, D. L. 2008, AJ, 135, 1039

Bickerton, S. J., Welch, D. L., & Kavelaars, J. J. 2009, AJ, 137, 4270

Box, G., & Pierce, D. 1970, Journal of the American Statistical Association, 1509

Chiang, E. I., & Brown, M. E. 1999, AJ, 118, 1411

Fuentes, C. I., & Holman, M. J. 2008, AJ, 136, 83

Gilliland, R. L., & Brown, T. M. 1992, PASP, 104, 582

Gladman, B., et al. 2002, Icarus, 157, 269

Gumbel, E. J. 1943, Ann. Math. Statistics, 14, 253

Høg, E., et al. 2000, A&A, 355, L27

Jewitt, D., & Luu, J. 1993, Nature, 362, 730

Kaiser, N., & Pan-STARRS Team. 2002, in BAAS, Vol. 34, 1304

Kenyon, S. J., & Bromley, B. C. 2004, Nature, 432, 598

Kim, D.-W., et al. 2009, MNRAS, 770

Lehner, M. J., et al. 2009, PASP, 121, 138

Luu, J., et al. 1997, Nature, 387, 573

Maíz-Apellániz, J., et al. 2004, ApJS, 151, 103

Nihei, T. C., et al. 2007, AJ, 134, 1596

Pan, M., & Sari, R. 2005, Icarus, 173, 342

Pasinetti Fracassini, L. E., et al. 2001, A&A, 367, 521

Reed, B. C. 2003, Aj, 125, 2531

Rice, J. 2007, Mathmatical Statistics and Data Analysis, 97

Roques, F., & Moncuquet, M. 2000, Icarus, 147, 530

Roques, F., Moncuquet, M., & Sicardy, B. 1987, AJ, 93, 1549

Roques, F., et al. 2006, AJ, 132, 819

Russell, H. N. 1916, ApJ, 43, 173

Scholz, M. 1997, in IAU Symposium, Vol. 189, 51–58

Skrutskie, M. F., et al. 2006, AJ, 131, 1163

Tonry, J., Burke, B. E., & Schechter, P. L. 1997, PASP, 109, 1154

Trujillo, C. A., et al. 2001, AJ, 122, 2740

Van Belle, G. T. 1999, PASP, 111, 1515

Wells, D. C., Greisen, E. W., & Harten, R. H. 1981, A&AS, 44, 363

Young, A. T. 1967, AJ, 72, 747

Zhang, Z.-W., et al. 2008, ApJL, 685, L157

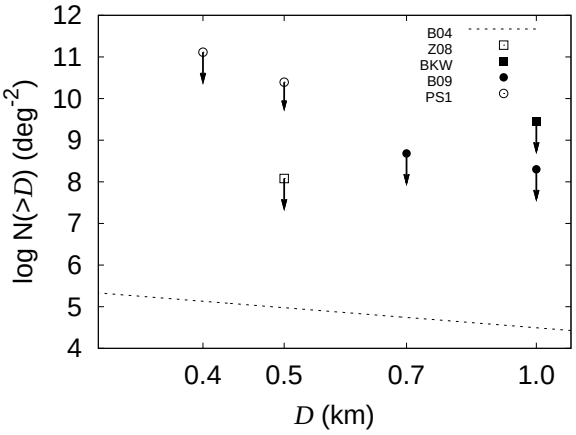

Fig. 17.—: The upper limit sets by PS1 22 star-hours engineering data at 95% confidence limit along with upper limits by TAOS, BKW (Bickerton et al. 2008) and B09 (Bianco et al. 2009).